

# Super-resolution optical imaging and memory enabled by scattering suppression of shell-coated gold nanorods

XIANGYU MA<sup>1,2,†</sup>, LE GAO<sup>1,2,3,†</sup>, LONGFANG YAO<sup>1,2</sup>, JING WANG<sup>1,2</sup>,  
HAOYI YU<sup>1,2</sup>, MIN GU<sup>1,2,4</sup> AND QIMING ZHANG<sup>1,2,\*</sup>

<sup>1</sup> School of Artificial Intelligence Science and Technology, University of Shanghai for Science and Technology, Shanghai 200093, China.

<sup>2</sup> Institute of Photonic Chips, University of Shanghai for Science and Technology, Shanghai 200093, China.

<sup>†</sup>These authors contributed equally to this work.

<sup>3</sup>e-mail: tzxfgl@163.com

<sup>4</sup>e-mail: gumin@usst.edu.cn

\*Corresponding author: qimingzhang@usst.edu.cn

Received XX Month XXXX; revised XX Month, XXXX; accepted XX Month XXXX; posted XX Month XXX (Doc. ID XXXXX); published XX Month XXXX

**Abstract:** Owing to sensitive nonlinear plasmonic responses, anisotropic metal nanoparticles are effective nanoprobes for optical imaging. However, the photo-thermal instability issues have hindered their further nanophotonics application potentials. In this letter, we reported the super-resolution imaging and optical memory through suppressing the plasmonic scattering signal of core-shell gold nanorods (GNRs). Good thermal stability and conductivity from GNRs coated with 20 nm silica shell supported the super-resolution imaging with a lateral feature size of 114 nm ( $\lambda/5.6$ ) via a very low suppressing laser power (0.9 mW). The GNRs were then employed for achieving super-resolved bio-imaging with a feature size of 128 nm ( $\lambda/5$ ). More importantly, we were able to realize the super-resolution optical recording (feature size: 173 nm) in a GNRs-polyvinyl alcohol sample. This work further extends our understanding as well as the nanophotonics application of core-shell anisotropic metal nanoparticles based on nonlinear plasmonic scattering.

## 1. Introduction

Far-field super-resolution microscopy techniques including stimulated emission depletion microscopy (STED), stochastic optical reconstruction microscopy and photo-activated localization microscopy have been developed over the past two decades to provide abundant information of biological objects with a resolution beyond the diffraction limit of light via fluorescent nanoprobes/dyes [1,2]. Issues such as high energy consumption of the laser sources, phototoxicity to the observed bio-samples, photobleaching and low photostability of fluorescent nanoprobes regrettably surround the aforementioned techniques. Plasmonic nanoparticles, however, can offer attractive factors such as high photostability, bright signals at low energy consumption, tunable optical responses, low phototoxicity due to the material compositions, excellent localized surface plasmon resonance (LSPR) and scattering features [3]. Consequently, as an alternative to organic dyes or quantum dots, plasmonic nanoparticles have been explored as novel non-fluorescent schemes for far-field super-resolution microscopy [4,5]. In addition, noble metal nanoparticles (such as gold or silver) possess very strong Mie scattering signals [6] and they have been widely used in chemical and biological sensing [7] data storage [8–11] and photothermal imaging [12].

Upon the irradiation of an excitation light source, metal nanoparticles exhibit high optical sensitivity features including plasmonic scattering and LSPR due to the collective oscillation of free electrons and considerably large electric field enhancement [13,14].

Relevant studies have shown that the nonlinear behavior of plasmonic scattering of metal nanoparticles is credited to the light absorption enhanced by plasmon and the subsequent thermal effect [15]. The photo-thermal nonlinearity features of plasmonic scattering is the foundation of realizing super-resolution nano-imaging. Spatial information can be extracted from the nonlinear elements of the plasmonic scattering upon the incident Gaussian shaped excitation laser source to obtain microscopic imaging of the metal nanoparticles via time modulation and demodulation process [16]. The scattered light outside the effective excited laser spot can be suppressed by the inhibition laser beam (in a donut shape) in a dual-beam STED microscope fashion, thereby improving the resolution of individual nanoparticles up to the sub-diffraction level [17]. The nonlinear plasmonic scattering in noble metal nanoparticles with various shapes and forms such as nanospheres [18], nanorods [19], and nanostars [20] has been extensively studied for micro/nano-imaging. Both isotropic shaped gold nanospheres [21] and anisotropic shaped gold nanostars [5] were employed for non-fluorescence-based super-resolution optical imaging. A recent study on shell-coated gold nanospheres has discovered that local heat dissipation plays a key role in nonlinear plasmonic scattering [4]. The photothermal stability can be significantly improved by coating the nanoparticles with silica shell, and the plasmon coupling caused by inter-particle aggregation can be effectively reduced. A recent study demonstrated that pulsed lasers are sufficient to induce photothermal nonlinear effects in plasmonic nanoparticles [18]. Furthermore, the gold nanospheres used in the study required larger time constant for signal demodulation, which results in low-speed nano-imaging. Fast point scanning can likely lead to incomplete signal demodulation, causing line-by-line drift and slow nano-imaging when using nanospheres. This limitation can be mitigated by employing nanoparticles with faster and stronger scattering intensity. In comparison, anisotropic gold nanoparticles exhibit enhanced extinction cross-sections at resonance wavelengths and elevated scattering intensities (Fig. S2), attributed to their tunable aspect ratios and tip-induced "hot spots" with significantly enhanced localized electric fields [22]. Simultaneously, anisotropic nanostructures like gold nanorods (GNRs) typically exhibit broader LSPR spectral coverage, including the near-infrared (NIR) biological transparency window (Fig. S3), making them superior candidates for low-power and rapid nano-imaging implementations [23]. Promising as they seem to be, naked GNRs tend to melt and lose their excellent nonlinear plasmonic response upon the incident laser beam due to their high thermal sensitivity yet low thermal stability, hence inhibiting their application potential in the field of nanophotonics. To the best of our knowledge, the research on solving the pressing thermal stability issue of anisotropic GNRs for unlocking their potential in super-resolution imaging and optical memory applications has not been investigated yet [24]. Furthermore, the previous works of metal nanoparticles for optical memory application have not been shown to reach beyond diffraction limit barrier [8–11].

In this letter, we characterized and compared the plasmonic scattering response and thermal stability of GNRs coated with silica shell of different thicknesses (0 to 40 nm) through the irradiation of a Gaussian-shaped picosecond pulsed laser beam (640 nm). The local thermal conductivity and thermal stability of GNRs coated with different silica shell thickness were discovered to exert significant effect on plasmonic scattering response. STED-like microscope imaging method, i.e. suppression of scattering imaging (SUSI) [17] was employed to perform super-resolution optical imaging of GNRs in a dual-beam configuration (a Gaussian shaped laser source (640 nm) for excitation and a donut shaped laser source (760 nm) for inhibition). After the aforementioned characterization processes, core-shell GNRs with 20 nm silica shell thickness were selected for their balanced thermal stability, high plasmonic response and low energy consumption for the ensued super-resolution imaging and laser writing application. Using SUSI imaging method, a lateral feature size (the full width at half maximum (FWHM) distribution of the plasmonic

scattering signal) as small as 114 nm ( $\sim\lambda/5.6$ ) was achieved in a single core-shell GNR with a suppressing laser power at 0.9 mW. Two adjacent core-shell GNRs with sub-diffraction distances can be super-resolved respectively as well (feature sizes: 122 nm and 157 nm). SUSI microscopy method was then utilized to conduct nano-imaging of a HeLa cell bio-sample doped with GNRs, proving the feasibility of applying core-shell GNRs for bio-imaging scenario. More significantly, we were able to demonstrate the super-resolution optical information recording (lateral feature size of 173 nm) in a solid film sample of polyvinyl alcohol (PVA) doped with the core-shell GNRs, surpassing the Abbe diffraction limit of the single-beam direct laser writing system by two times. Equipped with great thermal conductivity and highly sensitive nonlinear plasmonic scattering features, our research of core-shell GNRs represents a feasible pathway for future application of plasmonic anisotropic core-shell nanoparticles in super-resolution bio-imaging and optical recording. Further study of the sub-diffraction modulation of plasmonic scattering mechanism in GNRs-based optical information writing aspect can potentially lead to super-resolution photoinduced-inhibition nanolithography (SPIN) scheme [25], opening up broader nanophotonics applications such as nanoscale optical disk [26] and nanophotonic devices.

## 2. Methods

Fig. 1(a) illustrates the schematic of the super-resolution optical imaging method i.e. SUSI microscopy with core-shell GNRs as plasmonic nanoprobe. The experimental device is based on the Abberior STED super-resolution optical microscopy system, equipped with a 640 nm Gaussian-shaped pulsed laser beam (pulse width: 100 ps) and a 775 nm doughnut-shaped pulsed laser beam (pulse width: 1.3 ns). Both lasers have a repetition frequency of 40 MHz. Plasmonic scattering of the core-shell GNRs is excited by the 640 nm laser beam and is suppressed or inhibited by the 775 nm laser beam, generating an effective PSF function at super-resolution level. The naked GNRs and GNRs coated with silica shells of different thicknesses in our characterization and measurements were purchased from Kiko Bio, Nanjing. The transmission electron microscope (TEM) image from Fig. 1(b) shows one representative type of core-shell GNRs used in our experiments. Each one of the GNRs consists of a core GNR with an average longitudinal diameter of  $85 \pm 3$  nm and a latitudinal diameter of  $24 \pm 2$  nm (an aspect ratio of 3.5), and it is coated with a silica shell with a thickness of  $20 \pm 2$  nm. The peak of the LSPR signal from the longitudinal direction of the GNRs is 760 nm. The core-shell GNR sample was dispersed and fixed on a cover glass with the help of PVA. Core-shell GNRs were mixed with 20% aqueous solution of PVA, and the resulting mixture was ultrasonically treated at room temperature for 3 h to reach a uniform dispersion. The uniformly dispersed mixture was then deposited on a cover glass and spin coated at 1000 rpm for 30 seconds, and dried at 60 °C for 2 minutes to obtain a dry state sample. The sample was placed on the Olympus IX83 microscope translation stage, imaged with an objective (100 $\times$ , NA=1.4, oil 1 immersion) from the Abberior STED microscopy system. The to-be-observed backscattered signal of the nanoparticles is detected through a time-gate control device (gate delay: 850 ps, gate width: 8 ns) and a single-photon avalanche diode (SPAD) detector located behind the confocal pinhole, as shown in Fig. 1(c). The gating of both lasers and the SPAD is triggered by a synchronized transistor-transistor logic (TTL) signal from the same patch module from the Abberior microscope system. The signal was processed via a software from the microscope system (ImInspector, Specim), and a sub-diffraction limited image was then obtained with a single pixel size of 10 nm $\times$ 10 nm and 10  $\mu$ s of residence time for each pixel. Based on a previous study of nonlinear plasmonic scattering induced by pulsed beam irradiation [5], the optimal excitation pulse width of gold nanoparticles is on a time scale of 20 ns. Therefore, all the optical switching and super-resolution imaging are measured when the nanoparticles have reached a state of thermal equilibrium.

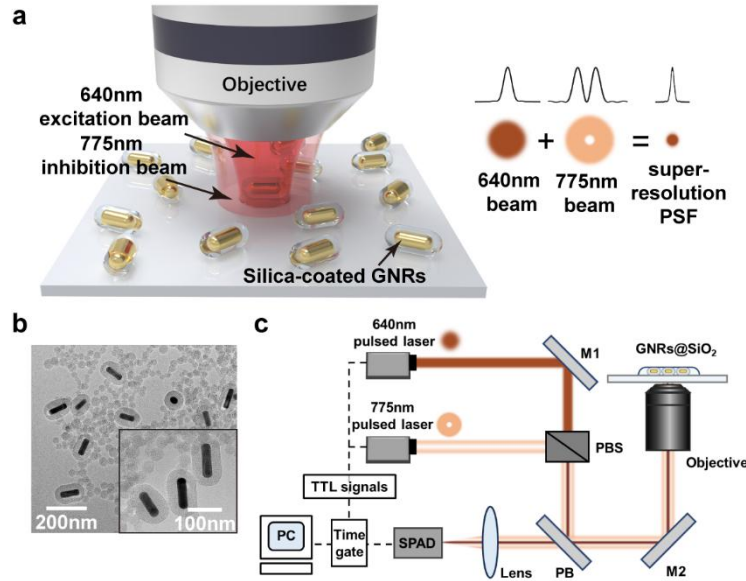


**Fig. 1.** (a) Schematics of super-resolution optical imaging via SUSI microscopy of core-shell GNRs as plasmonic scattering nanoprobe. A 640 nm Gaussian-shaped excitation laser beam, a 775 nm doughnut-shaped suppression laser beam and the effective super-resolution point spread function (PSF) are illustrated for the SUSI microscopy principle. (b) TEM imaging of 20 nm silica shell-coated GNRs. (c) Schematic diagram of the super-resolution optical system using a patch module to control double-pulse laser synchronization and time gate in the time domain.

### 3. Results

It is imperative to determine which plasmonic scattering peak of GNRs sample is the most suitable choice for the STED microscope system (a 640 nm laser for excitation and a 775 nm laser for inhibition) in order to conduct SUSI nano-imaging. Fig. 2(a) shows the measured absorption spectra (by UV-2600i spectrometer, Shimadzu) from custom ordered 4 types of naked GNRs (Kiko bio, Nanjing) with different plasmonic scattering peaks. The normalized absorption spectrum peaks, in direct correlation with the plasmonic scattering peaks [27], are at 640 nm, 680 nm, 720 nm and 760 nm for the corresponded longitudinal diameter sizes (57 nm, 63 nm, 72 nm and 84 nm, as shown in TEM images from Fig. S1 in Supplemental Document. See Supplement 1) and are at ~520 nm for the same latitudinal diameter size (~24 nm). The 4 types of GNRs samples were then co-irradiated by 640 nm and 775 nm laser (both in Gaussian shape). We fixed the power (0.5 mW) of the 640 nm laser to effectively saturate the intensity plasmonic scattering signal of the GNRs sample and slowly increased the power of inhibition 775 nm laser beam from zero to observe the inhibition effect. Fig. 2(b) shows the saturation inhibition (inhibition principle of SUSI nano-imaging) analysis of the plasmonic scattering signal of the four GNRs samples under the co-irradiation of 640 nm (fixed power at 0.5 mW) and 775 nm (increases from 0 mW) laser sources (both are in Gaussian shape). One can see that the GNRs sample with 760 nm plasmonic scattering peak (the purple dots and the purple fitting curve) has the fastest inhibition rate (highest slope) with the lowest inhibition power (0.6 mW for maximum inhibition) achieved among all four samples. Fig. 2(c) demonstrates the distribution of the intensity of plasmonic scattering signal from the four types of GNRs as the irradiation intensity of the inhibition 775 nm laser beam (Gaussian shape) increases. The intensity of

plasmonic scattering signal of the GNRs sample with 760 nm plasmonic scattering peak (the purple dots and purple fitting curve) is the highest compared to other GNRs samples since their scattering peak is the closest to the wavelength (775 nm) of the inhibition laser. In conclusion, the GNRs sample with the plasmonic scattering peak at 760 nm is most suited for low-power SUSI nano-imaging with the dual-beam STED microscope system set-up.

Then we conducted characterization tests and studied the thermal effect of core-shell GNRs samples (all with 760 nm plasmonic scattering peak) with different thicknesses of the silica shell (0 nm, 10 nm, 20 nm and 40 nm). Fig. 2(d) simulates the electric near-field spatial distribution of a bare GNR on a glass substrate upon the excitation of the 640 nm laser. The concentrated field intensity on the nanorod's both ends contribute to GNRs fast temperature rises upon optical illumination. The absorption spectra in Fig. S4 (Supplement 1) indicates that the plasmonic resonance peak of core-shell GNRs (20 and 40 nm silica shell) in aqueous solution undergoes a 'red shift' effect. This phenomenon is attributed to the higher refractive index of the silica shell compared to the surrounding aqueous medium, which modifies the local dielectric environment and induces a bathochromic displacement of the surface plasmonic resonance band according to Mie scattering theory. For shell thickness over 40 nm, no further migration is observed [28].

Fig. 2(e) shows the normalized distribution of the plasmonic scattering signal intensity of GNRs with four different silica shell thicknesses under laser irradiation at an excitation wavelength of 640 nm. The experimental results indicate that the bare GNRs reach scattering saturation first, orderly followed by those with 10 nm, 20 nm, and 40 nm silica shells. As the thickness of the silica shell increases, the laser power required to achieve plasmonic scattering saturation shows an increasing trend. The specific laser power values required to achieve plasmonic scattering saturation are 0.4 mW (0 nm), 0.46 mW (10 nm), 0.5 mW (20 nm), and 0.63 mW (40 nm), respectively. This phenomenon indicates that thicker silica shells require higher incident light energy to achieve plasmonic scattering saturation of the GNRs samples (the purple dots and the fitting curve).

Fig. 2(f) systematically studies the regulation of the plasmonic scattering characteristics of core-shell structured GNRs by the power of the 775 nm inhibition laser. Since the thermal conductivity of silica is better than that of oil, a thicker silica layer results in enhanced heat conduction effectiveness. As the silica shell thickness increases, its thermal conductivity approaches more closely to that of the glass. The experimental data indicate that as the inhibition laser power gradually increases from zero, the normalized plasmonic scattering intensity shows a significant positive correlation with the silica shell thickness. The bare GNRs reach the scattering saturation first, orderly followed by the core-shell GNRs with 10 nm, 20 nm, and 40 nm shells. The specific laser power values required to achieve saturation are 4.1 mW (0 nm), 4.6 mW (10 nm), 5.7 mW (20 nm), and 6.2 mW (40 nm), respectively. GNRs samples with thicker silica shells exhibit superior thermal conduction performance, requiring higher laser power energy to reach plasmonic scattering saturation. This indicates that the higher the temperature of the GNRs reach, the more readily they attain saturation. Thicker silica shell provides an effective heat dissipation pathway for the GNRs, significantly enhancing their thermal stability.

As shown in Fig. 2(g), we conducted the thermal diffusion modeling to simulate the relationship between nanoparticles' temperature and the incident laser (775 nm) power for GNRs with different silica shell thicknesses (simulation details and discussion are listed in Fig. S5 and Fig. S6 (Supplement 1)). Under the same incident laser power, GNRs in oil exhibited the highest temperature rise, while 40 nm silica shell GNRs experienced the lowest temperature rise. GNRs with higher thermal conductivity exhibit faster heat dissipation rates, consequently leading to lower temperature rise. The temperature evolution of a single GNR hence depends strongly on the thermal conductivity of the GNR's

surrounding environment. Benefited from the effective heat dissipation brought by the thermal conductivity of the silica shell, GNRs with thicker silica shell exhibit better thermal stability (slower temperature rise) under the excitation laser illumination [4].

It has been observed experimentally that when the excitation laser power exceeds 0.6 mW (approximately  $0.4 \text{ MW/cm}^2$ ), bare GNRs and GNRs@10 nm silica shells samples likely experienced the disappearance of plasmonic scattering features, leading to the significant loss of scattering signals, as shown in the left panel of Fig. 2(h). This phenomenon is attributed to the deformation or even fragmentation of the nanorods [29]. Through electron microscope observations, we have identified a laser-induced morphological transition towards spherical shapes in bare GNRs, as demonstrated in the right panel of Fig. 2(h). Furthermore, our investigations have discovered that GNRs with thin silica shells (10 nm) frequently exhibit non-uniform coating coverage and structural defects during the nanoparticle synthesis process. Consequently, both bare GNRs and thin shell GNRs tend to aggregate, whereas GNRs with shell thickness exceeding 20 nm maintain well-defined interparticle spacing, as shown in Fig. S7. These undesired drawbacks (such as clustering, aggregation and fusion) under the laser illumination can induce drastic changes to plasmonic properties of naked or thin silica shell GNRs, resulting the loss of imaging ability. In contrast, GNRs with 20 nm and 40 nm shells can withstand higher illumination power and maintain structural integrity, hence demonstrating a more stable imaging performance. This observation aligns with the previous report [2323]. Uncoated GNRs exhibit a ‘blue shift’ effect and the steep attenuation of resonance peaks under the increased laser power. This is from GNRs structural deformation where the longitudinal axis progressively shortens while the latitudinal axis expands, ultimately transforming into spherical shapes as illustrated in Fig. S8. Thin silica coatings offer merely partial protection, where hollow interfacial regions emerge between the GNR core and silica shell as the aspect ratio decreases. In contrast, 20 nm or thicker silica coatings can effectively protect GNRs under the irradiation of nanosecond pulses during experimental imaging process.

These characterization results further deepened our understanding of plasmonic scattering responses as well as photo-thermal properties of GNRs with various silica shell thicknesses. In summary, the thermal stability of silica-coated 760 nm GNRs can be significantly improved compared to bare 760 nm GNRs upon the saturation excitation of the 775 nm pulsed laser beam. However, as the thickness of the silica shell increases, higher laser power is required to achieve both saturation and inhibition of plasmonic scattering of the nanoparticles for effective SUSI super-resolution imaging. GNRs with a 20 nm shell thickness have been experimentally validated to possess sufficient thermal stability for our application requirements. Taking abovementioned factors into consideration, we chose 760 nm GNRs with 20 nm silica shell for the ensued nano-imaging, bio-imaging and laser writing tests because they can effectively balance the need for good thermal stability and low-power SUSI super-resolution imaging by the STED microscope system.



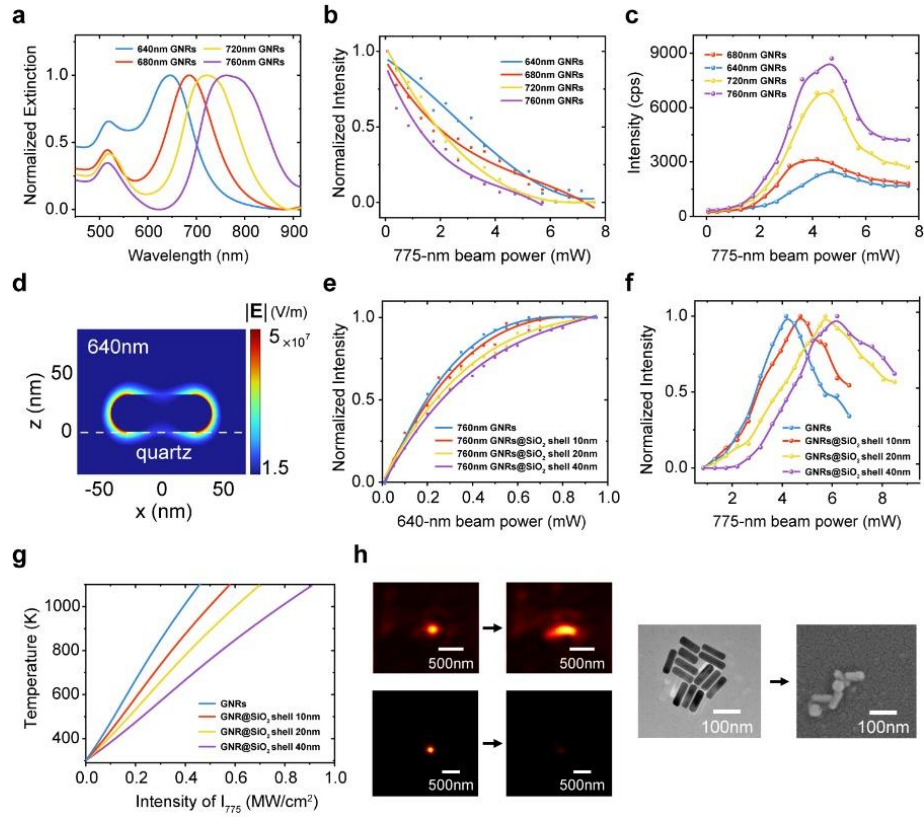


**Fig. 2.** (a) Normalized extinction spectra of bare GNRs with four different shapes. (b) The fitted scattering intensity distribution curves of four types of GNRs with different plasmonic scattering peaks under the co-irradiation of 640 nm (fixed power at 0.5 mW) and 775 nm (increases from 0 mW) laser sources. (c) The scattering intensity distribution curves of GNRs with different plasmonic scattering peaks under the irradiation of varying power of Gaussian-shaped 775 nm suppression laser beam. (d) Simulation of the spatial distribution of electric near-field of a bare GNR (760 nm plasmonic scattering peak) on a glass substrate upon the excitation of the 640 nm excitation laser. (e) The fitted normalized scattering intensity curves of the 4 types of GNRs with different shell thicknesses upon the irradiation of the 640 nm excitation laser. (f) The normalized scattering intensity distribution curve of the GNRs with different shell thicknesses as the illumination power of 775 nm inhibition laser increases from zero. (g) The relationship between nanoparticle temperature and incident laser power (775 nm) for GNRs with different silica shell thicknesses. (h) Example of photo-thermal instability issue for bare or thin silica shell coated GNRs in SUSI imaging (left panel) and the TEM image (right panel).

We then performed super-resolution imaging (SUSI method) of GNRs with a 20 nm thick silica shell based on the nonlinear plasmonic scattering behavior and the results are shown in Fig. 3. The 640 nm excitation laser beam (power: 0.17 mW) and the 775 nm donut-shaped suppression laser beam (power: 0.9 mW) were used for super resolution imaging of the GNRs sample. The FWHM values of GNRs images were obtained by fitting the distribution curve of plasmonic scattering signal. Fig. 3(a)(i) shows the scattering images of dispersed GNRs under confocal (left) and SUSI (right) imaging configurations. Fig. 3(a)(ii) compares the confocal and SUSI microscopy imaging of one isolated GNR in the selected region of Fig. 3(a)(i). The FWHM of Gaussian-fitted profile of the nanoparticle confocal imaging is 264 nm, while the FWHM of SUSI super-resolution imaging profile

(inhibition laser beam power: 0.9 mW) is compressed to 114 nm ( $\lambda/5.5$ ), improving the imaging resolution by 2.3 times. The power density in our SUSI imaging ( $6.4 \times 10^5 \text{ W/cm}^2$ ) is about three orders of magnitude less than a typical dye-based STED microscope ( $10^8 \text{ W/cm}^2$ ) [2]. Fig. 3(b) demonstrates that two adjacent GNRs at sub-diffraction distance can be resolved by SUSI microscopy imaging. The confocal imaging method cannot resolve the two closely located GNRs while SUSI imaging can clearly resolve the two GNRs (FWHM of the fitting profile of each GNR imaging: 122 nm and 157 nm respectively). The above super-resolution imaging results lays the foundation for the silica shell-coated GNRs as a nanoprobe option for non-fluorescence based super-resolution optical imaging

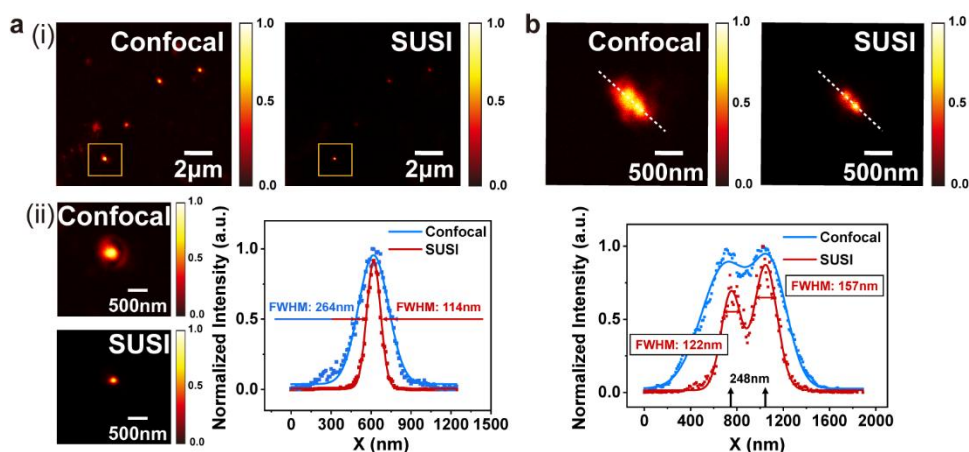


**Fig. 3.** Super-resolution imaging (SUSI method) of the selected core-shell GNRs. (a)(i) Confocal and SUSI microscope imaging of dispersed 20 nm thick silica shell-coated GNRs. The following figure (ii) shows the confocal and SUSI images of individual GNR and the corresponding normalized plasmonic scattering intensity profiles. The scattered dots are from confocal and SUSI im-aging measurements, and the solid lines are Gaussian fitting curves. (b) Confocal and SUSI imaging of two adjacent core-shell GNRs and the corresponding normalized plasmonic scattering intensity profiles (the figure below).

The application of core-shell GNRs in bio-imaging and direct laser writing is exhibited in Fig. 4. SUSI super-resolution optical imaging of GNRs in Hela cells sample was realized and shown in Fig. 4(a). The cell structure was scanned by confocal optical microscope and core-shell GNRs was scanned by SUSI super-resolution microscope. The Fig. 4(a)(i) contains confocal imaging of Hela cells with the green fluorescent protein marker Life Act-EGFP staining (left), GNRs staining (middle) and an enlarged confocal image (right) of dispersed core-shell GNRs that have entered the Hela cells. In Fig. 4(a)(ii) and Fig. 4(a)(iii), the super-resolution imaging of core-shell GNRs in Hela cells was achieved by SUSI microscopy at a 775 nm suppressing laser beam power of 0.9 mW ( $5.4 \times 10^5 \text{ W/cm}^2$ ). The FWHM of a single GNR profile can be super-resolved down to 128 nm and the resolution of two adjacent GNRs can be better distinguished via SUSI microscopy. Fig. 4(b) demonstrated the sub-diffraction optical recording in a solid-state sample which is a dried mixture (1:2 wt ratio) of core-shell GNRs aqueous solvent (10 mg/ml) and PVA water solvent (20%). A femtosecond (fs) laser writing system powered by an 800 nm laser (Solstice Ace, Spectra-Physics, pulse width: 100 fs, repetition rate: 5 kHz, writing power: 80 μW) was focused through an objective (Olympus, 1.4 NA, 100×) for sub-diffraction optical recording of a two-dimensional pattern “USST” in the solid PVA-GNRs sample. The super-resolution imaging of individual letters was achieved by SUSI micro-copy with



the FWHM of a lateral feature size compressed down to 173 nm ( $\lambda/3.7$ ), which is half of the Abbe diffraction limit (348 nm) of laser processing system. Direct laser writing of gratings and dots in the GNRs-PVA sample was also conducted via a 520 nm fs laser writing system (Carbide, Light Conversion, pulse width: 205 fs, repetition rate: 1MHz, objective: 0.95NA 100 $\times$ , writing power: 4.6  $\mu$ W) and two sub-diffraction limit gratings and dots were achieved (resolution: 235 nm) as shown in Fig. 4(c).

Notably, anisotropic gold nanoparticles not only facilitate the formation of additional LSPR modes but also exhibit strong polarization-dependent optical responses. As evidenced in prior investigations on multidimensional optical storage using GNRs [30], both plasmonic resonance wavelength and polarization state can serve as important physical dimensions for information multiplexing purpose. Although the GNRs' orientation is randomly distributed in our current super-resolution imaging and optical recording demonstrations, we still investigated the underlying influence of laser polarization direction on the orientation of anisotropic GNRs through simulations. As shown in Fig. S9, the strongest plasmonic enhancement effect occurs at  $\theta=\pi/2$ , when the polarization angle of the incident laser is aligned with the GNR longitudinal axial direction. This finding holds significant implications for super-resolution applications: Through ordered arrangement of anisotropic nanoparticles combined with precise polarization control of the incident laser beam, substantial enhancement can likely be realized in both imaging sensitivity and optical recording precision.

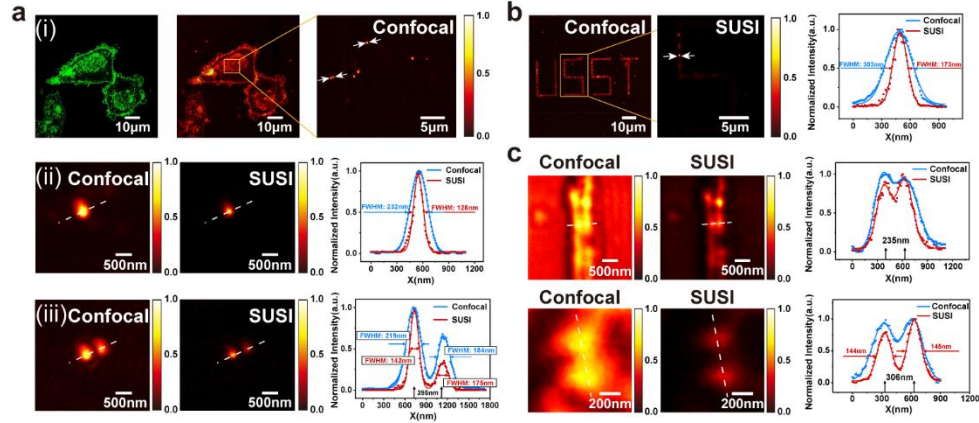


**Fig. 4.** Application of core-shell GNRs in super-resolution bio-imaging and optical recording. (a) (i) Confocal microscopy image of HeLa cells stained with Life Act-EGFP (left) and GNRs (right) and enlarged confocal image of GNRs (boxed region); (ii) Confocal and SUSI microscopy images of a single core-shell GNR from the box-selected region (indicated by white arrows) in the HeLa cell and the corresponding normalized intensity profiles of the plasmonic scattering signal; (iii) Confocal and SUSI microscopy images of two adjacent GNRs and the normalized intensity profiles of the plasmonic scattering signal. (b) Confocal and SUSI microscopy imaging of sub-diffraction optical recording of "USST" letters in a solid PVA-GNRs film sample. The analysis for the normalized scattering intensity profiles is on the right. (c) Confocal and SUSI microscopy images of laser recorded two adjacent gratings and two dots processed in the solid PVA-GNRs film sample and the corresponding normalized intensity profiles for the plasmonic scattering signal.

#### 4. Conclusion

In summary, we investigated the practical applications of core-shell GNRs for non-fluorescence far-field super-resolution imaging by pulsed-laser sources and sub-diffraction optical writing. Core-shell GNRs coated with different thicknesses of silica shell were

studied and characterized based on their nonlinear plasmonic scattering response, thermal stability and power consumption. It is proposed that GNRs with silica shells of 20 nm thickness possess balanced qualities including good plasmonic scattering response, high thermal stability, solid maintenance of structural integrity as well as low power consumption. We then used them as plasmonic nanoprobe for super-resolution optical imaging and achieved a lateral feature size of 114 nm ( $\lambda/5.6$ ). Core-shell GNRs have also been shown to enter biological cells and have rendered super-resolved bio-imaging possible. More importantly, we demonstrated the super-resolution optical information writing in a GNRs-PVA solid-state sample. This study extends the practical nano-imaging and recording scenarios of utilizing core-shell anisotropic metal nanoparticles based on nonlinear plasmonic responses. Further research into the SPIN writing mechanism of plasmonic scattering sensitive GNRs-based nanomaterials can be of considerable significance for nanoscale optical memory and nanophotonic devices applications.

**Funding.** National Key Research and Development Program of China (Grant No. 2022YFB2804300 and 2021YFB2802000), the Shanghai Municipal Science and Technology Major Project, the Shanghai Frontiers Science Center Program (2021-2025 No. 20), the Science and Technology Commission of Shanghai Municipality (Grant No. 21DZ1100500), the National Natural Science Foundation of China (Grant No. 61975123) and the Shanghai Science and Technology Innovation Action Plan (Grant No. 23JC1403100 and No. 24JD1402700).

**Disclosures.** The authors declare no conflicts of interest.

**Data Availability.** Data underlying the results presented in this Letter are not publicly available at this time but may be obtained from the authors upon reasonable request.

**Supplemental Document.** See [Supplement 1](#) for supporting content.

## References

1. S. Pujals, N. Feiner-Gracia, P. Delcanale, *et al.*, “Super-resolution microscopy as a powerful tool to study complex synthetic materials,” *Nat. Rev. Chem.* **3**, 68–84 (2019).
2. S. W. Hell and J. Wichmann, “Breaking the diffraction resolution limit by stimulated emission: stimulated-emission-depletion fluorescence microscopy,” *Opt. Lett.* **19**, 780–782 (1994).
3. K. M. Mayer and J. H. Hafner, “Localized Surface Plasmon Resonance Sensors,” *Chem. Rev.* **111**(6), 3828–3857 (2011).
4. T. Zhang, Z. Wang, X. Zhong, *et al.*, “Photothermal nonlinear scattering of shell-isolated gold nanoparticles and applications in super-resolution imaging,” *Chin. Opt. Lett.* **21**(10), 103601 (2023).
5. X. Zhang, J. Wang, S. Lamon, *et al.*, “Scattering suppression in plasmonic nanostars using pulsed-beam irradiation for super-resolution optical imaging,” *Opt. Lett.* **47**(16), 4223 (2022).
6. A. Wax and K. Sokolov, “Molecular imaging and darkfield microspectroscopy of live cells using gold plasmonic nanoparticles,” *Laser & Photon. Rev.* **3**(1-2), 146–158 (2009).
7. E. C. Dreaden, A. M. Alkilany, X. Huang, *et al.*, “The golden age: gold nanoparticles for biomedicine,” *Chem. Soc. Rev.* **41**(7), 2740–2779 (2012).
8. P. Zijlstra, J. Chon, and M. Gu, “Five-dimensional optical recording mediated by surface plasmons in gold nanorods,” *Nature* **459**, 410–413 (2009).
9. Q. Zhang, Z. Xia, Y. Cheng, *et al.*, “High-capacity optical long data memory based on enhanced Young’s modulus in nanoplasmonic hybrid glass composites,” *Nat. Commun.* **9**, 1183 (2018).
10. M. Gu, X. Li, and Y. Cao, “Optical storage arrays: a perspective for future big data storage,” *Light Sci. Appl.* **3**, e177 (2014).
11. X. Li, T.-H. Lan, C.-H. Tien, *et al.*, “Three-dimensional orientation-unlimited polarization encryption by a single optically configured vectorial beam,” *Nat. Commun.* **3**, 998 (2012).
12. Y. Tang, T. Yen, K. Nishida, *et al.*, “Mie-enhanced photothermal/thermo-optical nonlinearity and applications on all-optical switch and super-resolution imaging [Invited],” *Opt. Mater. Express.* **11**(11), 3608–3626 (2021).
13. H. Yu, Y. Peng, Y. Yang, *et al.*, “Plasmon-enhanced light–matter interactions and applications,” *npj Comput. Mater.* **5**, 45 (2019).
14. J. Wang, L. Zhang, and M. Qiu, “Nonlinear plasmonics: second-harmonic generation and multiphoton photoluminescence,” *Photonix* **4**, 32 (2023).
15. I. W. Un and Y. Sivan, “Thermo-optic nonlinearity of single metal nanoparticles under intense continuous wave illumination,” *Phys. Rev. Mater.* **4**, 105201 (2020).
16. K. Nishida, G. Deka, N. I. Smith, *et al.*, “Nonlinear Scattering of Near-Infrared Light for Imaging Plasmonic Nanoparticles in Deep Tissue,” *ACS Photonics* **7**(8), 2139–46 (2020).

17. H. Wu, Y. Huang, P. Shen, *et al.*, "Ultrasmall all-optical plasmonic switch and its application to super-resolution imaging," *Sci. Rep.* **6**, 24293 (2016).
18. C. Li, Y. Li, Y. Han, *et al.*, "Pulsed Saturated Absorption Competition Microscopy on Nonbleaching Nanoparticles," *ACS Photonics* **7**(7), 1788 (2020).
19. J. Zheng, X. Cheng, H. Zhang, *et al.*, "Gold Nanorods: The Most Versatile Plasmonic Nanoparticles," *Chem. Rev.* **121**(21), 13342–13453 (2021).
20. F. Hao, C. L. Nehl, H. Jason, *et al.*, "Plasmon Resonances of a Gold Nanostar," *Nano Lett.* **7**(3), 729–732 (2007).
21. J. Xu, T. Zhang, S. Yang, *et al.*, "Plasmonic Nanoprobes for Multiplexed Fluorescence-Free Super-Resolution Imaging," *Adv. Opt. Mater.* **6**(20), 1800432 (2018).
22. J. Zuloaga, E. Prodan, P. Nordlander, "Quantum Plasmonics: Optical Properties and Tunability of Metallic Nanorods," *ACS Nano* **4**(9), 5269–5276 (2010).
23. Y. Chen, W. Frey, S. Kim, *et al.*, "Enhanced thermal stability of silica-coated gold nanorods for photoacoustic imaging and image-guided therapy," *Opt. Express* **18**(9), 8867–8878 (2010).
24. H. Geng, S. V. Pedersen, Y. Ma, *et al.*, "Noble Metal Nanoparticle Biosensors: From Fundamental Studies toward Point-of-Care Diagnostics," *Acc. Chem. Res.* **55**(5), 593–604 (2022).
25. Z. Gan, Y. Cao, R. Evans, *et al.*, "Three-dimensional deep sub-diffraction optical beam lithography with 9 nm feature size," *Nat. Commun.* **4**, 2061 (2013).
26. M. Zhao, J. Wen, Q. Hu, *et al.*, "A 3D nanoscale optical disk memory with petabit capacity," *Nature* **626**, 772–778 (2024).
27. J. Cao, T. Sun and K. T. V. Grattan, "Gold nanorod-based localized surface plasmon resonance biosensors: A review," *Sens. Actuators B: Chem.* **195**, 332–351 (2014).
28. I. Pastoriza-Santos, J. Pérez-Juste, and L. M. Liz-Marzán, "Silica-Coating and Hydrophobation of CTAB-Stabilized Gold Nanorods," *Chem. Mater.* **18** (10), 2465–2467 (2006).
29. S. Link, C. Burda, B. Nikoobakht, *et al.*, "Laser-Induced Shape Changes of Colloidal Gold Nanorods Using Femtosecond and Nanosecond Laser Pulses," *J. Phys. Chem. B* **104** (26), 6152–6163 (2000).
30. X. Ouyang, Y. Xu, M. Xian, *et al.*, "Synthetic helical dichroism for six-dimensional optical orbital angular momentum multiplexing," *Nat. Photon.* **15**, 901–907 (2021).